Unveiling the Anomalous Photovoltaic Effect of Ferroelectric Domain Walls in $BiFeO_3$ Thin Films

Jianjun Lin,[1] Yuang Chen,[1] Hongru Wang,[1] Bobo Tian,[1] Ye Chen,[1] Zhiyong Zhou,[2] Fangyu Yue,[1] Rong Huang,[1,*] Chun-Gang Duan,[1] Junhao Chu,[1,3] and Lin Sun[1,†]

[1] *Key Laboratory of Polar Materials and Devices (MOE), Department of Electronics, East China Normal University, Shanghai 200241, China*

[2] *Shanghai Institute of Ceramics, Key Laboratory of Inorganic Functional Materials and Devices, Chinese Academy of Sciences, 1295 Dingxi Road, Shanghai 200050, People's Republic of China*

[3] *Institute of Optoelectronics, Fudan University, Shanghai 200438, China*

(Received 16 September 2022; revised 8 December 2022; accepted 11 January 2023; published 17 February 2023)

The presence of ferroelectric domain walls (DWs) can generate an above-band-gap photovoltage of a ferroelectric photovoltaic device, which is the anomalous photovoltaic (APV) effect, and its mechanism is still under debate. Here, the effective electric field and the local bulk photovoltaic (BPV) component at 71° DWs are reported by quantitatively analyzing the light polarization angle-dependent photovoltaic effect of nonperiodic DWs and periodic stripe DWs in $BiFeO_3$ films. The photovoltaic measurement under white light illumination directly reveals a significantly enhanced electric field at stripe DWs in comparison with the domains. The BPV effect at stripe DWs is about 25 times as large as that of the domains. Furthermore, the defect states at the DWs may recombine the photogenerated carriers and drastically weaken the electric field of the DWs, whereas they negligibly mitigate the BPV effect. This work offers a deeper insight into the mechanism of the APV effect at ferroelectric DWs.

DOI: 10.1103/PhysRevApplied.19.024050

I. INTRODUCTION

The photovoltaic (PV) effect in ferroelectric (FE) materials has attracted substantial attention owing to its photovoltage being significantly higher than the band gap and its switchable photocurrent under an alternating current electric field [1–6]. The PV response of the FE device with coplanar-electrode structure involves two mechanisms: the bulk photovoltaic (BPV) effect [6–8] arising from noncentrosymmetry, and the domain wall photovoltaic (DWPV) effect [4,9] stemming from a spatial rotation of spontaneous polarization across domain-wall (DW) regions. Ferroelectric DWs, which feature unique properties, such as conduction, magnetoelectric coupling, and anomalous photovoltaic (APV) effect, are homogeneous boundaries that separate different orientations of electric polarization [4,10–13]. The fascinating functionalities of DWs are believed to hold potential for applications as functional elements in nanodevices. Intensive studies have been performed for FE oxides in multidomain (MD) states because the presence of DWs can significantly enhance the PV response [9,10,14,15]. However, the previous viewpoints on the origin of the APV effect in MD state FE oxides is not consistent, especially in $BiFeO_3$ (BFO) thin films.

Recent studies on BFO with stripe DWs have proposed that the high photovoltage under white illumination originates from an electrostatic potential step at the DWs [4]. However, white light illumination, due to the random distribution of light polarization, does not enable the investigation of the BPV effect in stripe DW samples. Subsequently, the temperature-dependent PV properties have been demonstrated by Bhatnagar *et al.*, revealing that BFO films generate a markedly high photovoltage thanks to the reduced conductivity of the DWs at low temperature [10]. They consider BPV theory as the main mechanism of the PV effect in MD samples, rather than the electrostatic potential step at the DWs. High conductivity at DWs seems to be detrimental to the PV effect of MD samples [10]. More recently, the effect of 71° DWs on the PV effect was described in BFO films grown epitaxially on $SrTiO_3$ (STO) substrates with a miscut angle of 4° along with the [110] ($STO_{4°\,[110]}$) and [100] ($STO_{4°\,[100]}$) directions, revealing the dominance of the DWPV effect over the BPV effect [16]. This result agrees with the conclusion in the $BaTiO_3$ (BTO) system of MD states with 90° domain structures [9,15]. However, the method of using a $STO_{4°\,[100]}$ substrate to get a 71° domain structure results in nonperiodic DWs, which is not completely consistent

*rhuang@ee.ecnu.edu.cn
†lsun@ee.ecnu.edu.cn

with the theoretical model of periodic stripe domains. Furthermore, the contribution of the DWPV effect is indirectly derived from the offset term of the BPV equation and lacks direct experimental support. Most recently, detecting terahertz radiation in BFO films, a new method to probe the PV response, suggested the dominant contribution of DWs compared with the PV response in the single-domain (SD) sample [17]. Terahertz measurement, however, is unable to directly observe and further quantitatively analyze the DW-mediated PV mechanism. Therefore, the specific APV mechanism of DWs in BFO thin films with periodic stripe-patterned domains remains controversial.

To address this problem, BFO thin films with SD, periodic stripe, and nonperiodic 71° domains are grown by pulsed laser deposition (PLD). The BPV tensors obtained in the SD sample enable the direct demonstration and quantitative evaluation of the APV effect at the DWs, which contain both strong electric field and BPV component. We employ the PV measurement under white light illumination, which directly indicates the high electric field generated by electrostatic potential drops at the DWs. The defects at the DWs may be responsible for the relatively low electric field under white light illumination. In combination with the aberration-corrected scanning transmission electron microscopy (STEM) and temperature-dependent PV measurements, we argue that the enhanced light polarization angle-dependent photocurrent (BPV effect) at the DWs is caused by the stronger spatial symmetry breaking at the DWs.

II. RESULTS AND DISCUSSION

A. Thin-film fabrication and domain characterization

First, to study the domain difference between the BFO thin films grown on $STO_{4^\circ\,[100]}$ and (110)-oriented $DyScO_3$ (DSO) substrates, domain analysis is conducted by piezoresponse force microscopy (PFM) and reciprocal space mapping (RSM). Details of film growth are given in Appendix 1. Figure 1 shows the results with the corresponding schematics to clearly emphasize the differences between two kinds of 71° domains. Figure 1(a) shows the in-plane domain morphology of two structural variants with 71° domains on $BFO/STO_{4^\circ\,[100]}$, which are presented with nonperiodic domains with variable sizes (100–1000 nm). The topography image shows the step surface, and the terrace width is approximately 200 nm [see Supplemental Material Fig. S1(a)] [18]. Figures 1(b) and 1(c) display the RSMs around STO (103) and (013) reflections for BFO films. The double diffraction peak of (103) indicates the existence of MD structures in BFO films on the $STO_{4^\circ\,[100]}$ substrates, which is consistent with the PFM. The RSM also shows that the BFO peak is slightly away from the black dashed vertical line, indicating that the BFO films on the $STO_{4^\circ\,[100]}$ substrates are relaxed.

On the other hand, the in-plane PFM image of BFO films on (110)-oriented DSO substrates shows the periodic 71° stripe-pattern domains [see Fig. 1(e)]. The surface of the BFO films on the DSO substrates is atomically smoother with larger terrace width (about 1 μm) than that on $STO_{4^\circ\,[100]}$ substrates [see Supplemental Material Fig. S1(b)] [18]. The RSM patterns around (103) and (013) reflections for the BFO films on the DSO substrates are shown in Figs. 1(f) and 1(g), respectively. An obvious splitting of BFO peaks is observed in Fig. 1(f), which confirms the presence of two-variant structural domains in BFO films. The RSM shows the fully strained BFO films on the DSO substrates because of their closer lattice match with DSO than $STO_{4^\circ\,[100]}$. The peak width of the BFO films on the DSO substrates is much narrower along the (010) direction, indicating the improvement of crystalline quality in the BFO films by using DSO substrates. Out-of-plane x-ray diffraction (XRD) shows the strong (00l) ($l = 1$, 2, and 3) diffraction peaks of the BFO films, proving the formation of a single-crystalline BFO phase [see Supplemental Material Figs. S1(c) and S1(d)] [18]. Additionally, we fabricate the BFO films on the $STO_{4^\circ\,[110]}$ substrates to obtain SD structures as a reference, and the SD structure characterization is shown in the Supplemental Material Figs. S1(e)–S1(h) [18]. Figures 1(d) and 1(h) show schematic diagrams of the domain structures of BFO films on $STO_{4^\circ\,[100]}$ and DSO substrates, respectively. We use the laboratory coordinate (x,y,z) system to define the measurement direction of the PV effect. The $[010]_{pc}$ and $[001]_{pc}$ (subscript pc represents pseudocubic setting) directions are 4° away from the y and z axes for the $BFO/STO_{4^\circ\,[100]}$ sample, and the $[100]_{pc}$ and $[010]_{pc}$ directions are parallel to x and y axes for the BFO/DSO sample. The ferroelectric polarization is also marked in Figs. 1(d) and 1(h). The BFO film grown on the TiO_2-terminated STO substrate can cause $SrO\text{-}TiO_2/BiO\text{-}FeO_2$ interface leading to the upward ferroelectric polarization of BFO [19,20]. The DSO substrate after the thermal annealing process results in the upward polarization of BFO, as shown in our STEM images. These findings reveal that BFO films on DSO substrates exhibit more periodic 71° stripe domains. The DWs with periodic stripe patterns would be more useful for extracting the DW contribution to the PV properties of BFO films.

B. Anomalous photovoltaic effect at domain walls

To comprehensively understand the mechanism of the APV effect at 71° DWs of BFO films, we perform a detailed PV study of BFO films on $STO_{4^\circ\,[100]}$ and DSO substrates with nonperiodic and periodic domain patterns, respectively. We also investigate the PV response of the $BFO/STO_{4^\circ\,[110]}$ sample with SD state for reference (see Supplemental Material Fig. S2) [18]. In the following, we mark the $BFO/STO_{4^\circ\,[110]}$, $BFO/STO_{4^\circ\,[100]}$,

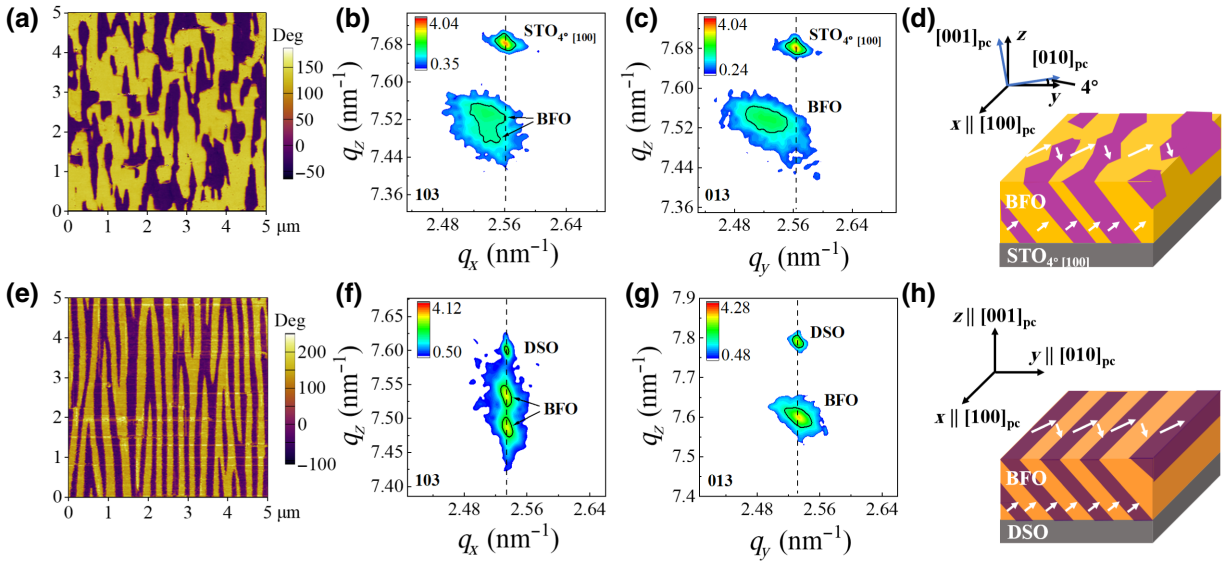

FIG. 1. Ferroelectric domain characterization of MD samples. In-plane PFM phase images (5×5 μm^2) show the multidomain structure with 71° domain walls for 200-nm-thick BFO films on (a) $STO_{4^\circ\,[100]}$ and (e) DSO substrates. RSM images around (103) reflections for BFO films on (b) $STO_{4^\circ\,[100]}$ and (f) DSO substrates. RSM images around (013) reflections for BFO films on (c) $STO_{4^\circ\,[100]}$ and (g) DSO substrates. The values given for the color legends represent intensity in arbitrary units. Schematics of the multidomain structure of (d) BFO/$STO_{4^\circ\,[100]}$ and (h) BFO/DSO. The white arrows indicate the components of polarization direction in each domain. The relationship between the orthorhombic, pseudocubic, and laboratory-coordinate (x,y,z) axes is shown.

and BFO/DSO samples as SD, MD-STO, and MD-DSO samples, respectively. Figures 2(a) and 2(d) show the configuration of the PV measurement of MD-STO and MD-DSO samples, respectively. All samples are measured under illumination with linearly polarized light ($\lambda = 405$ nm). The light polarization direction is controlled by a half-wavelength plate. Linearly polarized light propagates along the z axis with a light polarization angle θ from the y axis in the x-y plane. We define the short-circuit current density (J_{SC}) along the r axis ($r = x, y$) as $J_{r,MD-STO}$ or $J_{r,MD-DSO}$ and the corresponding open-circuit voltage (V_{OC}) as $V_{r,MD-STO}$ or $V_{r,MD-DSO}$ in the MD sample, and denote them as $J_{r,SD}$ and $V_{r,SD}$ in the SD sample. Supplemental Material Fig. S3 shows the current density–bias voltage (J-V_{bias}) characteristics of the SD ($\theta = 60°$ for $J_{-x,SD}$ and $\theta = 0°$ for $J_{-y,SD}$), MD-STO ($\theta = 40°$ for $J_{x,MD}$ and $\theta = 0°$ for $J_{y,MD}$), and MD-DSO ($\theta = 40°$ for $J_{x,MD}$ and $\theta = 0°$ for $J_{y,MD}$) samples at a range of light intensities, which confirm a linear relation between J and V_{bias} [18]. J_{SC} reaches the maximum value at these light polarization angles. Figures 2(b) and 2(c) exhibit the absolute value of J_{SC} ($|J_{SC}|$) and V_{OC} ($|V_{OC}|$) as a function of thickness-averaged light intensity (I_{opt}) for the MD-STO sample, and Figs. 2(e) and 2(f) show those for the MD-DSO sample. I_{opt} is expressed by film thickness (d), incident light intensity (I_{in}), and absorption coefficient ($\alpha = 2.1 \times 10^5$ cm^{-1}) as $I_{opt} = I_{in}\frac{1-\exp(-\alpha d)}{\alpha d}$ [7]. The $|J_{SC}|$ varies linearly with increasing I_{opt}, and $|V_{OC}|$ reaches saturation when I_{opt} is greater than around 20 W cm^{-2}. Hence, we discuss the PV effect at $I_{opt} = 35$ W cm^{-2}, where V_{OC} is independent of I_{opt}. The MD-DSO sample shows a larger $V_{y,MD-DSO}$ (16.7 V) than that of the MD-STO sample (12.3 V), and a relatively small $V_{x,MD-DSO}$ (0.6 V) compared with that of the MD-STO sample (3.7 V). The reason for the higher $V_{y,MD}$ value of the MD-DSO sample is the periodic stripe domains and increased DW density, whereas the disordered distribution of DWs and inconsistent domain widths in the MD-STO sample reduce the $|V_{OC}|$. This observation reveals the role of periodic stripe domains in the MD-DSO sample and can better explain the contribution of DWPV effects. $J_{y,MD}$ and $V_{y,MD}$ in both MD samples are much larger than those in the SD sample, indicating the remarkable contribution of DWs to increasing the J_{SC} and V_{OC}. Additionally, we calculate the photoconductivity ($\sigma_{ph} = |J_{SC}/E_{OC}|$), where E_{OC} is the open-circuit electric field, i.e., $E_{OC} = V_{OC}/L$ (L is electrode distance), from the slope of the J-V_{bias} data in the y direction for the SD and MD samples. σ_{ph} is proportional to I_{opt} and the values of σ_{ph}/I_{opt} for the y direction configuration are shown in Table I. Since σ_{ph}/I_{opt} values in the y direction configuration are very close, the σ_{ph} of 71° DWs does not dominate the APV effect at room temperature. This result is in agreement with the previous report [16].

Next, we need to obtain the BPV tensor to quantitatively assess the contribution of the APV effect at the DWs. The J-V_{bias} characteristics of the SD, MD-STO, and MD-DSO samples under linearly polarized light ($\theta = 0°$–$180°$) show the linear relation between J and V_{bias} (see Supplemental

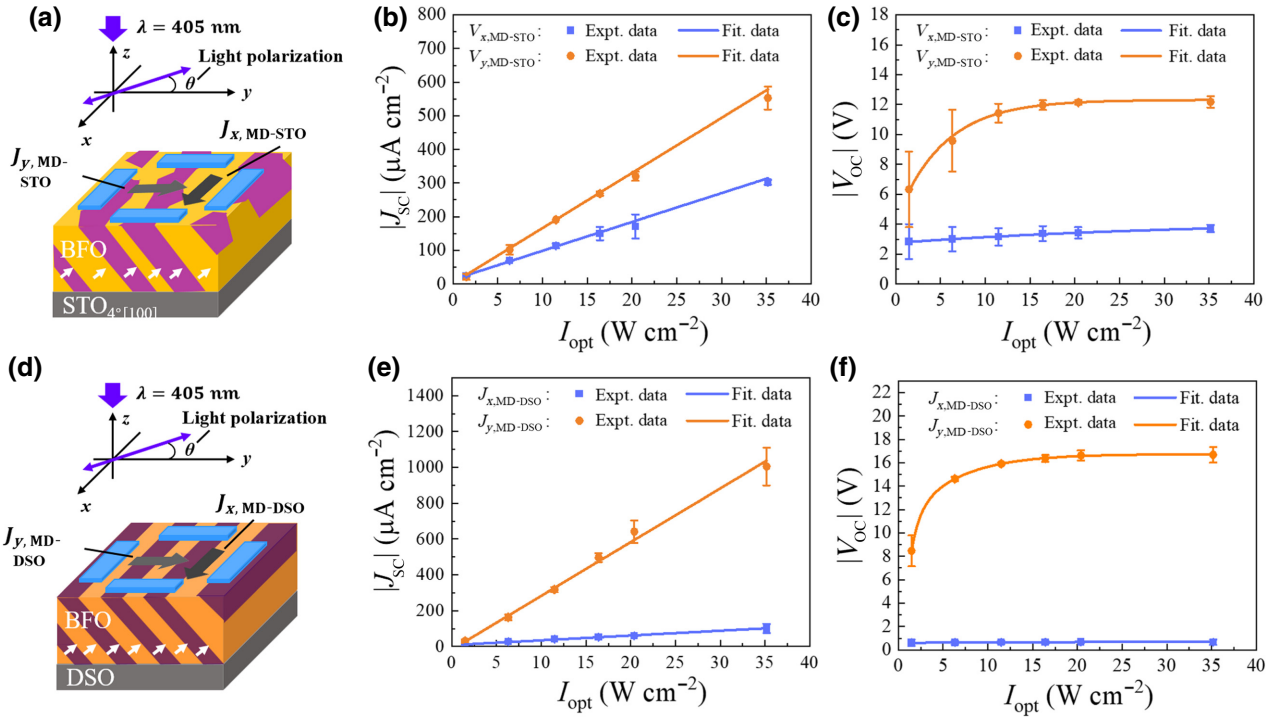

FIG. 2. Photovoltaic properties of MD samples under different light intensities. Configuration of the PV measurement of (a) MD-STO and (d) MD-DSO samples. Short-circuit current density (J_{SC}) as a function of thickness-averaged light intensity (I_{opt}) for (b) the MD-STO and (e) MD-DSO samples. Open-circuit voltage (V_{OC}) as a function of I_{opt} for (c) the MD-STO and (f) MD-DSO samples. The solid lines are the fitting data.

Material Fig. S4) [18]. To get the BPV tensor elements, we first analyze the sinusoidal dependence of J_{SC} on θ extracted from the J-V_{bias} features in the SD sample (see Supplemental Material Fig. S5) [18], because the role of DWs is ruled out in the SD sample. Figure 3(a) shows the schematic of the PV measurement under linearly polarized light. When the SD sample is illuminated with linearly polarized light, J_{SC} originates from the BPV effect. $J_{-x,SD}$, and $J_{-y,SD}$ can be expressed as follows:

$$J_{-x,\text{SD}}/I_{\text{opt}} = \beta^{\text{bulk}}_{-x,\text{SD,amp}} \sin(2\theta + \varphi), \quad (1)$$

$$J_{-y,\text{SD}}/I_{\text{opt}} = \beta^{\text{bulk}}_{-y,\text{SD,off}} + \beta^{\text{bulk}}_{-y,\text{SD,amp}} \cos(2\theta + \varphi), \quad (2)$$

where $\beta^{\text{bulk}}_{-x,\text{SD,amp}}$, $\beta^{\text{bulk}}_{-y,\text{SD,amp}}$, and $\beta^{\text{bulk}}_{-y,\text{SD,off}}$ indicate the sinusoidal and offset tensor components of the BPV effect of the SD sample, respectively. φ is an experimental phase shift, i.e., the experimental angle error of $\theta = 0°$, which represents the initial misalignment between the polarized light and the in-plane ferroelectric polarization. The specific expressions for $\beta^{\text{bulk}}_{-x,\text{SD,amp}}$, $\beta^{\text{bulk}}_{-y,\text{SD,amp}}$, and $\beta^{\text{bulk}}_{-y,\text{SD,off}}$, taking into account the influence of the 4° miscut angle, are shown in the Supplemental Material Eqs. (S8), (S9), and (S10) (see Ref. [18]) [16]. The elements of the BPV tensor, obtained by fitting the statistical data of $J_{-x,SD}$ and $J_{-y,SD}$ [see Supplemental Material Figs. S5(e) and S5(f)] using Eqs. (1) and (2), are listed in Table II. For the MD sample, we assume that $J^{\text{bulk}}_{y,\text{MD}}$ is determined by the BPV effect alone, which can be described by

$$J^{\text{bulk}}_{y,\text{MD}}/I_{\text{opt}} = \beta^{\text{bulk}}_{y,\text{MD,off}} - \beta^{\text{bulk}}_{y,\text{MD,amp}} \cos(2\theta + \varphi), \quad (3)$$

where $\beta^{\text{bulk}}_{y,\text{MD,amp}}$ and $\beta^{\text{bulk}}_{y,\text{MD,off}}$ indicate the sinusoidal and offset tensor components of the BPV effect of the MD sample, respectively. Here, $\varphi = 0°$ theoretically. The specific expressions of $\beta^{\text{bulk}}_{y,\text{MD,amp}}$ and $\beta^{\text{bulk}}_{y,\text{MD,off}}$ for MD-STO and MD-DSO samples are shown in the Supplemental Material Eqs. (S15), (S16), (S19), and (S20) (see Ref. [18]). The BPV tensor of the SD sample determines $\beta^{\text{bulk}}_{y,\text{MD-STO,amp}} = -5.9 \times 10^{-6}$ V^{-1} and $\beta^{\text{bulk}}_{y,\text{MD-STO,off}} = -6.2 \times 10^{-6}$ V^{-1} for the MD-STO sample, and $\beta^{\text{bulk}}_{y,\text{MD-DSO,amp}} = -5.5 \times 10^{-6}$ V^{-1} and $\beta^{\text{bulk}}_{y,\text{MD-DSO,off}} = -7.5 \times 10^{-6}$ V^{-1} for the MD-DSO sample.

TABLE I. The photoconductivity (σ_{ph}) characteristics along the y axis of the SD, MD–STO, and MD–DSO samples.

	SD	MD–STO	MD–DSO
J_{SC}/I_{opt} (μA W^{-1})	11.6	16.4	30.1
E_{OC} (V cm^{-1})	1376	2428	3325
σ_{ph}/I_{opt} (nS cm W^{-1})	8.4	6.7	9.0

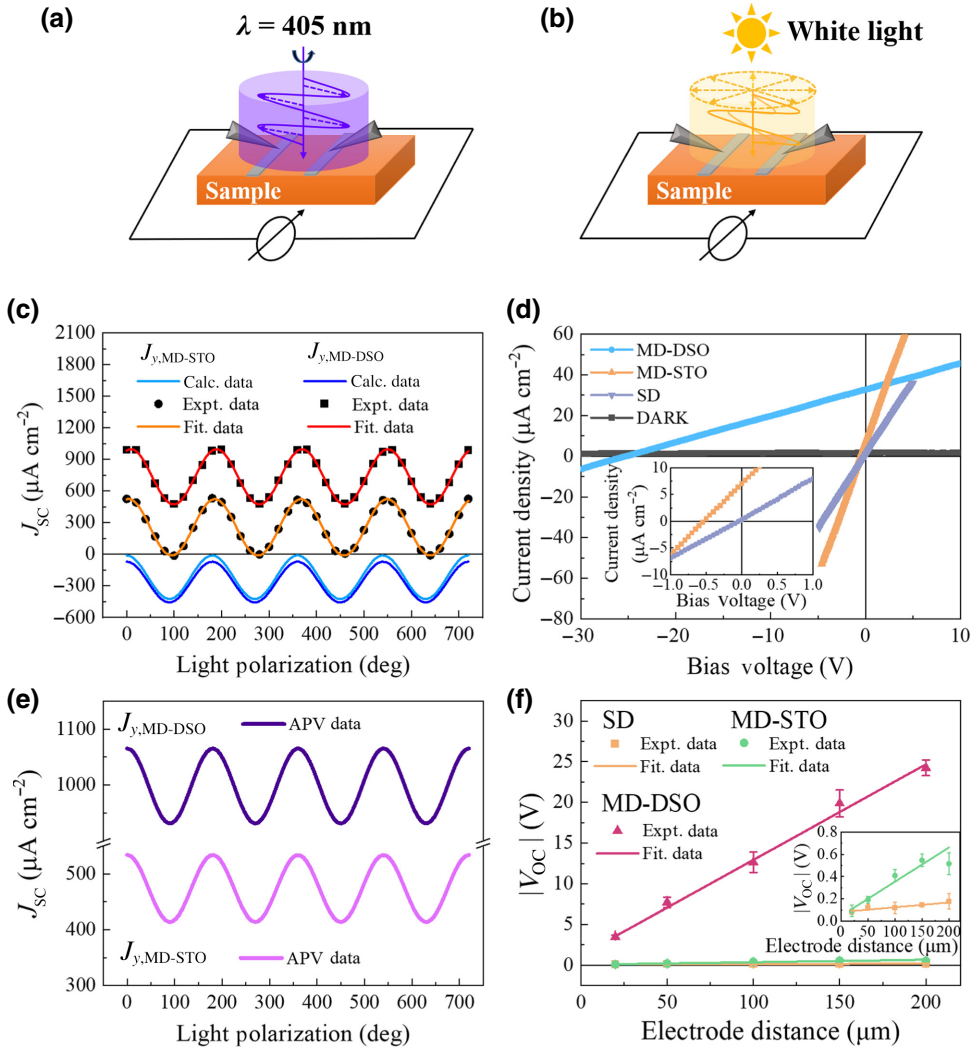

FIG. 3. Photovoltaic properties under linearly polarized light and white light illumination. Schematics of PV measurement under (a) linearly polarized light and (b) white light illumination. Under white light illumination, the J_{SC} of the MD sample is in the same direction as the in-plane polarization. (c) θ dependence of $J_{y,MD}$ for the MD-STO and MD-DSO samples. The black dots and squares are experimental data. The two solid blue lines are the theoretically calculated data, and solid red and orange lines are the sinusoidal fitting data. (d) J-V_{bias} characteristics along the y axis for the SD, MD-STO, and MD-DSO samples measured under white light illumination (about 0.4 W cm^{-2}) at an electrode distance of 200 μm. The inset shows an enlarged image of J-V_{bias} near zero bias for SD and MD-STO samples. (e) The APV data of DWs for the MD-STO (solid pinkish-purple line) and MD-DSO (solid purple line) samples are obtained by subtracting the calculated data from the experimental data in (c). (f) The $|V_{OC}|$ dependence of L along the y axis under white light illumination. The inset shows enlarged data for SD and MD-STO samples.

In Fig. 3(c), we plot the $J^{bulk}_{y,MD-STO}$ and $J^{bulk}_{y,MD-DSO}$ curves theoretically calculated using Eq. (3) (two blue lines) when the APV effect of the DWs is not considered. The fitting curves for the experimental data (solid red and orange lines) are also shown in Fig. 3(c). In comparison, although the calculated curves display negative offset and

TABLE II. Elements of the BPV tensor of the SD sample, and the APV effect (β^{DW}_{off} and β^{DW}_{amp}) of DWs for the MD-STO and MD-DSO samples.

	β_{15} (V^{-1})	β_{22}(V^{-1})	β_{31}(V^{-1})	β_{33}(V^{-1})	$\beta^{DW}_{y,MD,off}$(V^{-1})	$\beta^{DW}_{y,MD,amp}$(V^{-1})
SD	1.3×10^{-5}	-4.9×10^{-6}	2.8×10^{-7}	-4.9×10^{-5}		
MD-STO	1.3×10^{-5}	-4.9×10^{-6}	2.8×10^{-7}	-4.9×10^{-5}	1.3×10^{-5}	-1.7×10^{-6}
MDDSO	1.3×10^{-5}	-4.9×10^{-6}	2.8×10^{-7}	-4.9×10^{-5}	2.8×10^{-5}	-1.9×10^{-6}

sinusoidal components, the experimental curves show positive offset and larger sinusoidal components. These results demonstrate that the PV effect of the MD samples arises from not only the BPV effect of the domains but also the APV effect of the DWs. Thus, we should modify $J_{y,\mathrm{MD}}$ by

$$J_{y,\mathrm{MD}}/I_{\mathrm{opt}} = (\beta^{\mathrm{DW}}_{y,\mathrm{MD,off}} + \beta^{\mathrm{bulk}}_{y,\mathrm{MD,off}}) - (\beta^{\mathrm{DW}}_{y,\mathrm{MD,amp}} + \beta^{\mathrm{bulk}}_{y,\mathrm{MD,amp}})\cos(2\theta+\varphi), \quad (4)$$

where $\beta^{\mathrm{DW}}_{y,\mathrm{MD,amp}}$ and $\beta^{\mathrm{DW}}_{y,\mathrm{MD,off}}$ indicate the sinusoidal and offset tensor components of DWs, respectively. The statistics of the experiment [see Supplemental Material Figs. S5(g) and S5(h)] [18] can be well fitted by Eq. (4), and the fitted values of $\beta^{\mathrm{DW}}_{y,\mathrm{MD,amp}}$ and $\beta^{\mathrm{DW}}_{y,\mathrm{MD,off}}$ for the MD-STO and MD-DSO samples are listed in Table II. To directly visualize the APV effect of DWs, we assume that $\varphi = 0°$ and plot the curve for the MD-STO (solid pinkish-purple line) and MD-DSO (solid purple line) samples obtained by subtracting the theoretically calculated data from the experimental data, as shown in Fig. 3(e). Thus, the curves of Fig. 3(e) actually demonstrate the APV data of the DWs for the MD-DSO and MD-STO samples. The contribution of $\beta^{\mathrm{DW}}_{y,\mathrm{MD,off}}$ is obvious and its value is positive. In particular, $\beta^{\mathrm{DW}}_{y,\mathrm{MD,off}}$ of the MD-DSO sample is much larger than that of the MD-STO sample. Therefore, the role of the DWPV effect for the MD-DSO sample with 71° periodic stripe domains is greater than that for the MD-STO sample. Furthermore, the apparent $\beta^{\mathrm{DW}}_{y,\mathrm{MD,amp}}$ indicates that DWs also exhibit the BPV effect.

C. Domain-wall photovoltaic effect

To quantitatively evaluate the contribution of DWs to the $\beta^{\mathrm{DW}}_{y,\mathrm{MD,off}}$, we calculate the effective electric field ($\tilde{E}_{y,\mathrm{MD}}$), which is the spatial gradient of the electrostatic potential. According to the relation of $J_{y,\mathrm{MD}} = I_{\mathrm{opt}}\beta = \sigma_{\mathrm{ph}}\tilde{E}_{y,\mathrm{MD}}$, the $\tilde{E}_{y,\mathrm{MD}}$ is given by [9,15]

$$\tilde{E}_{y,\mathrm{MD}} = \frac{(\beta^{\mathrm{DW}}_{y,\mathrm{MD,off}} + \beta^{\mathrm{bulk}}_{y,\mathrm{MD,off}})I_{\mathrm{opt}}}{\sigma_{\mathrm{ph}}}. \quad (5)$$

For the MD-DSO sample, the value of $\tilde{E}_{y,\mathrm{MD\text{-}DSO}}$ is calculated to be 2.3 kV cm^{-1}, which is twice as large as $\tilde{E}_{y,\mathrm{MD\text{-}STO}} = 1.1$ kV cm^{-1} for the MD-STO sample. Assuming that f^{DW} is the volume fraction of 71° DWs, then $\tilde{E}_{y,\mathrm{MD}}$ can be expressed as follows [15]:

$$\tilde{E}_{y,\mathrm{MD}} = (1-f^{\mathrm{DW}})\tilde{E}^{\mathrm{bulk}}_{y,\mathrm{MD}} + f^{\mathrm{DW}}\tilde{E}^{\mathrm{DW}}_{y,\mathrm{MD}}, \quad (6)$$

where $\tilde{E}^{\mathrm{bulk}}_{y,\mathrm{MD}}$ is the effective field inside the domains originating from the BPV effect and $\tilde{E}^{\mathrm{DW}}_{y,\mathrm{MD}}$ is the local field in the DW region arising from the DWPV effect. f^{DW} is written as w^{DW}/W, where w^{DW} is the average width of 71° DWs and W is the average DW spacing. From the PFM data, the W value is estimated to be around 150 nm for the MD-DSO sample. It is noted that estimating the W value of the MD-STO sample is not feasible because of the disordered DWs with varied domain widths. According to the STEM images (Fig. 4) and previous report, we assume that the w^{DW} value of MD-DSO sample is about 2 nm [21]. From this we calculate the f^{DW} value is 1/75. Therefore, the $\tilde{E}^{\mathrm{DW}}_{y,\mathrm{MD}}$ value of the MD-DSO sample is given as 239 kV cm^{-1}, which is 2 orders of magnitude higher than $\tilde{E}^{\mathrm{bulk}}_{y,\mathrm{MD}}$ (-0.8 kV cm^{-1}). This result shows that $\tilde{E}^{\mathrm{DW}}_{y,\mathrm{MD}}$ dominates the PV effect in the MD sample, causing the observed positive offset [15].

AM1.5G white light as a whole is nonpolarized, due to the random distribution of light-polarization directions. Under white light illumination, the light-polarization-dependent BPV effect can cancel out in all directions and only the light-polarization-independent response (i.e., the offset tensor component) remains. Thus, to directly obtain the built-in electric field at the DW, the PV measurement under white light illumination is employed and the schematic is shown in Fig. 3(b). J-V_{bias} characteristics along the x axis are shown in the Supplemental Material Fig. S6 [18]. In the x direction, the J-V_{bias} curves of the MD-DSO sample show small $|V_{\mathrm{OC}}|$, while the SD and MD-STO samples only exhibit photoconductivity. Figure 3(d) shows J-V_{bias} properties along the y axis for the SD, MD-STO, and MD-DSO samples measured in the dark and under white light illumination at an electrode distance of 200 μm (the J-V_{bias} characteristics with electrode distances of 20–150 μm are shown in the Supplemental Material Fig. S6 [18], and Fig. 3(f) shows the corresponding $|V_{\mathrm{OC}}|$ as a function of L along the y axis. Figure 3(d) shows that $|V_{\mathrm{OC}}|$ of the MD-DSO sample is noticeably larger than that of MD-STO sample, but there is no $|V_{\mathrm{OC}}|$ for the SD samples. The $|V_{\mathrm{OC}}|$ of the MD-STO and MD-DSO samples features a linear relation with L [Fig. 3(f)]. Surprisingly, the average electric field ($\tilde{E}'_{y,\mathrm{MD}} = |V_{\mathrm{OC}}|/L$) of the BFO/DSO sample (1.2 kV cm^{-1}) is 2 orders of magnitude higher than that of the MD-STO sample (0.03 kV cm^{-1}). From the W value of the MD-DSO sample, we further calculate the potential drop for each DW to be 18 mV ($\tilde{E}'_{y,\mathrm{MD}}W$), which is consistent with previous experimental and theoretical reports [4,11]. Conversely, the $|V_{\mathrm{OC}}|$ of the SD sample is negligible, which indicates that the BPV effect is not responsible for the PV response of the SD sample under white light illumination. Hence, the significant $\tilde{E}'_{y,\mathrm{MD}}$ originates from the DW, and the strongly enhanced $\tilde{E}'_{y,\mathrm{MD\text{-}DSO}}$ value results from the ordered 71° DWs and increased DW density.

It is worth noting that the $\tilde{E}_{y,\mathrm{MD\text{-}DSO}}$ value (2.3 kV cm^{-1}) under 405-nm polarized light illumination is increased compared with $\tilde{E}'_{y,\mathrm{MD\text{-}DSO}}$ (1.2 kV cm^{-1}) under white light and, more obviously, the $\tilde{E}_{y,\mathrm{MD\text{-}STO}}$ value (1.1 kV cm^{-1})

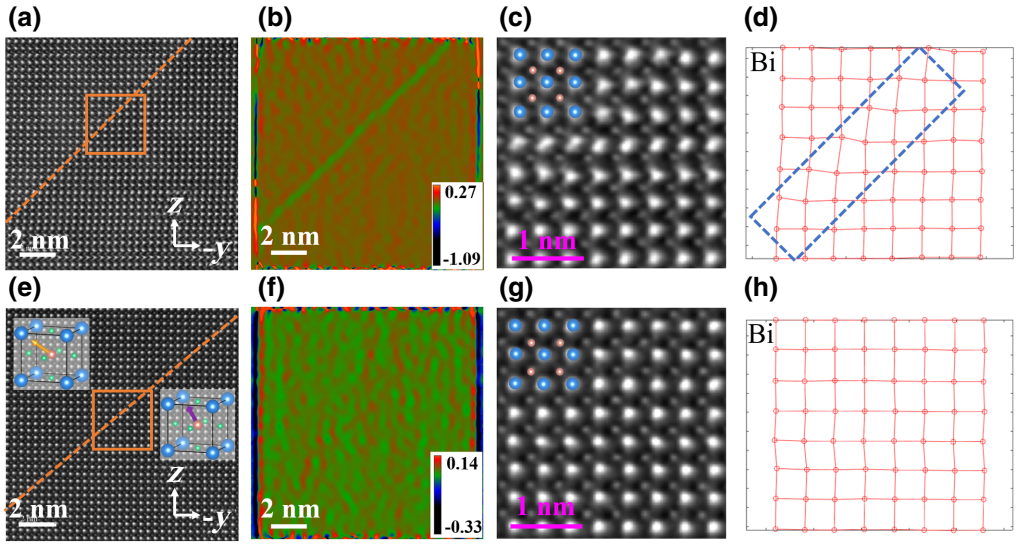

FIG. 4. STEM measurement of BFO films. Typical HAADF-STEM images of the (a) MD-STO and (e) MD-DSO samples with 71° DW corresponding to the areas labeled by the orange rectangle in the Supplemental Material Figs. S8(d) and S8(h) [18]. The orange dashed line indicates the 71° DW. (b),(f) Corresponding in-plane strain (ε_{xx}) maps of (a),(e) extracted via the GPA analyses. The values given for the color legends represent intensity in arbitrary units. The scale bar is 2 nm. (c),(g) Enlarged HAADF-STEM images from the rectangular regions in (a),(e). The scale bar is 1 nm. (d),(h) Bi sublattice quantitatively analyzed from the orange box in (a),(e). The blue and orange dots in (c),(e),(g) correspond to the Bi and Fe columns, and the green dots in (e) indicate the O columns.

obtained under polarized light illumination is significantly larger than $\tilde{E}'_{y,\text{MD-STO}}$ (0.03 kV cm^{-1}) obtained under white light illumination. What gives rise to this interesting phenomenon? This might be caused by the existence of a higher defect concentration in the DW of the MD-STO sample than that in the MD-DSO sample.

It should be emphasized that the white light illumination ($0.4 \times 12\% = 0.048$ W cm^{-2}, as only 12% of the solar spectrum can be absorbed) is low injection, whereas the polarized light illumination (35 W cm^{-2}) is high injection. In the-low injection condition, Shockley-Read-Hall (SRH) recombination is dominant for the real semiconductors with unavoidable defect states in the band gap. Alternatively, radiative recombination and Auger recombination become the dominant mechanisms in the high-injection condition [22]. Under white light illumination, almost all photogenerated carriers recombine because the density of defect states in the DWs of the MD-STO sample is comparable with the photogenerated carrier density, which makes V_{OC} approach close to zero. For the case of high injection, i.e., under strongly polarized light illumination, the photogenerated carrier concentration is 2 orders of magnitude higher than that of defect states and thus the electron Fermi level ($E_F{}^n$) and hole Fermi level ($E_F{}^p$) shift significantly into the conduction and valence bands, respectively. This means that all defect states in the band gap are occupied by electron and hole pairs and SRH recombination can be neglected in the high-injection condition. Consequently, radiative and Auger recombination govern the DWs of the MD-STO sample under strongly polarized light illumination and inevitably lead to the higher photovoltage, i.e., the large electric field at the DWs. The case of MD-DSO is similar, but the MD-DSO sample with a much lower defect concentration still produces a large V_{OC} even under white light illumination. To further confirm the defect-filled model, we also measure the $|V_{\text{OC}}|$ as a function of L along the y axis under 405-nm monochromatic light illumination (3.7 W cm^{-2}), as shown in the Supplemental Material Fig. S7 and Table S1 [18]. The measured results demonstrate that the photovoltage and electric field at the DWs increase when the defect states at the DWs are gradually filled by photoexcited carriers.

Hence, these observations indicate that the local field in the DW region dominates the PV response of the MD samples, and the MD-DSO sample has a much larger contribution from the DWs compared with the MD-STO sample. The reason for the enhanced electric field in the MD-DSO sample is the more ordered DWs with narrow domain spacing and relatively low defect concentration. These results strongly suggest the prominent role of periodic stripe DWs with higher DW density and fewer DW defects in enhancing the DWPV effect.

D. Bulk photovoltaic effect at domain walls

On the other hand, to assess accurately the contribution of DWs on $\beta^{\text{DW}}_{y,\text{MD,amp}}$, we evaluate $\beta^{\text{DW}}_{y,\text{MD,amp}}/w^{\text{DW}}$ as -9.5 V^{-1} cm^{-1} for the MD-DSO sample and -8.5 V^{-1} cm^{-1} for the MD-STO sample, respectively. The value is about 25 times as large as that inside the domains

$[\beta^{\text{bulk}}_{y,\text{MD,amp}}/(W - w^{\text{DW}}) = -0.37\ \text{V}^{-1}\ \text{cm}^{-1}$ for the MD-DSO sample], suggesting that the DW possesses a stronger BPV effect than the domain. Moreover, the almost identical $\beta^{\text{DW}}_{y,\text{MD,amp}}/w^{\text{DW}}$ values for the MD-DSO and MD-STO samples indicate that the periodicity of the DWs has little effect on the contribution to the BPV effect.

To understand the enhanced $\beta^{\text{DW}}_{y,\text{MD,amp}}$, we further characterize and analyze the atomic structure of 71° DWs in both MD samples. Supplemental Material Fig. S8 shows typical low-magnification high-angle annular dark-field (HAADF)-STEM and corresponding low-angle annular dark-field (LAADF)-STEM images of the MD-STO and MD-DSO samples viewed along the $[100]_{\text{pc}}$ zone axis [18]. The domain structures for the MD-STO sample can be observed from both the HAADF and LAADF images, as shown in the Supplemental Material Figs. S8(a)–S8(d) [18]. In contrast, the domain structures for the MD-DSO sample cannot be observed directly from the HAADF images [see Supplemental Material Figs. S8(e) and S8(g)] [18]. They can only be discerned from the strain contrast in the LAADF images, as shown in the Supplemental Material Figs. S8(f) and S8(h) [18]. This indicates that the DW structures are different for these two samples, though both are 71° DW. Figures 4(a) and 4(e) show the atomic-resolved HAADF-STEM images of the selected area labeled with the orange rectangle in the Supplemental Material Figs. S8(d) and S8(h), and the corresponding LAADF-STEM images are shown in the Supplemental Material Figs. S9(a) and S9(d) [18]. The polarization direction is determined by the opposite direction of displacement of the Fe ion from the center of the four Bi neighbors [23–26]. It is seen that Fe moves to the lower right with respect to its four nearest Bi neighbors [along the out-of-plane direction, Fig. 4(e)], indicating the upper-left polarization directions in MD-DSO sample. To visualize the variation of DWs, the corresponding in-plane (ε_{xx}) and out-of-plane (ε_{yy}) strain maps are extracted by geometric phase analysis (GPA), as shown in Figs. 4(b), 4(f), and Supplemental Material Fig. S9 [18]. The in-plane [Fig. 4(b)] and out-of-plane strain [see Supplemental Material Fig. S9(b)] of the MD-STO sample present an abrupt change at the DW, while no lattice distortion can be detected in the MD-DSO sample [Fig. 4(f) and Supplemental Material Fig. S9(e)] [18]. Figures 4(c) and 4(g) show the enlarged HAADF-STEM images of the rectangular area in Figs. 4(a) and 4(e), where Bi (blue dots) and Fe (orange dots) ions can be directly distinguished. Then the Bi sublattices are quantitatively analyzed and mapped in Figs. 4(d) and 4(h). It is clear that the distortion of the Bi lattice at the DW in the MD-STO sample is greater than that in the MD-DSO sample. Because the projections of the in-plane components of the 71° DW in the MD-DSO sample overlap along the electron-beam direction, they cannot be visualized along the $[100]_{\text{pc}}$ axis [Fig. 4(h)]. This observation is in agreement with the previous literature [21]. The obvious lattice distortion at the DW (blue box) in the MD-STO sample [Fig. 4(d)] is consistent with the GPA result. The inhomogeneous strain distribution and generation of noticeable lattice distortion at the DWs of the MD-STO samples may be related to the relatively high defect concentration, such as oxygen vacancies and dislocations [21,27–29], leading to a severe decrease in the $|V_{\text{OC}}|$ value of the MD-STO sample under white light illumination.

Based on these observations, we suggest that the greater centrosymmetry breaking at the DWs is the reason for the significant enhancement of $\beta^{\text{DW}}_{y,\text{MD,amp}}$ compared with that of domains, and thus causes a large $\beta^{\text{DW}}_{y,\text{MD,amp}}/w^{\text{DW}}$ value. Meanwhile, the similar atomic distribution characteristics of DWs for MD-DSO and MD-STO samples are responsible for the almost identical $\beta^{\text{DW}}_{y,\text{MD,amp}}$ values, irrespective of the DW periodicity. Moreover, we study the influence of temperature variation on σ_{ph} (see Supplemental Material Fig. S10), which further confirms the BPV nature in MD samples [18].

E. Mechanism discussion

Finally, to gain better insight into the APV effect of DWs, schematic illustrations of the stripe-patterned 71° DWs and the corresponding band diagram of the MD sample are shown in Fig. 5. The MD sample displays 71° ferroelectric variants and leads to various polarization directions in the x-y plane [Figs. 5(a) and 5(e)]. For the MD-DSO sample, as expressed in Eq. (6), the effective electric field $\tilde{E}^{\text{bulk}}_{y,\text{MD}}$ (-0.8 kV cm^{-1}) appears inside the domains, while the particularly larger $\tilde{E}^{\text{DW}}_{y,\text{MD}}$ (239 kV cm^{-1}) provides a steep gradient in the DW region [Fig. 5(c)] under polarized light illumination. Even though the DW region is extremely thin, the positive field of $\tilde{E}^{\text{DW}}_{y,\text{MD}}$ exceeds the negative one of $\tilde{E}^{\text{bulk}}_{y,\text{MD}}$, and thereby the short-circuit current is reversed by introducing 71° DWs [9,15,16]. Meanwhile, according to the PV effects under white light illumination, $\tilde{E}'_{y,\text{MD}}$ is estimated to be 1.2 kV cm^{-1} in the MD-DSO sample, which is 2 orders of magnitude larger than that in the MD-STO samples (30.7 V cm^{-1}). Under open-circuit illumination conditions, the electric field decreases at the DW with respect to its thermal equilibrium value due to the drift of photogenerated carriers to the other side of the DW, leading to a potential drop of about 18 mV [Fig. 5(d)]. The existence of defect states at the DW leads to the recombination of photogenerated carriers and results in the reduction of $|V_{\text{OC}}|$ in the MD-DSO sample, and especially in the MD-STO samples with high defect concentration where $|V_{\text{OC}}|$ is almost zero. Furthermore, the experimentally measured J_{sc} (approximately 33 μA cm^{-2}) of the MD-DSO sample is very close to the estimated value of about 37 μA cm^{-2} obtained from the DW model, indicating that the proposed model is reasonable (see details in the Supplemental Material Fig. S11 [18]).

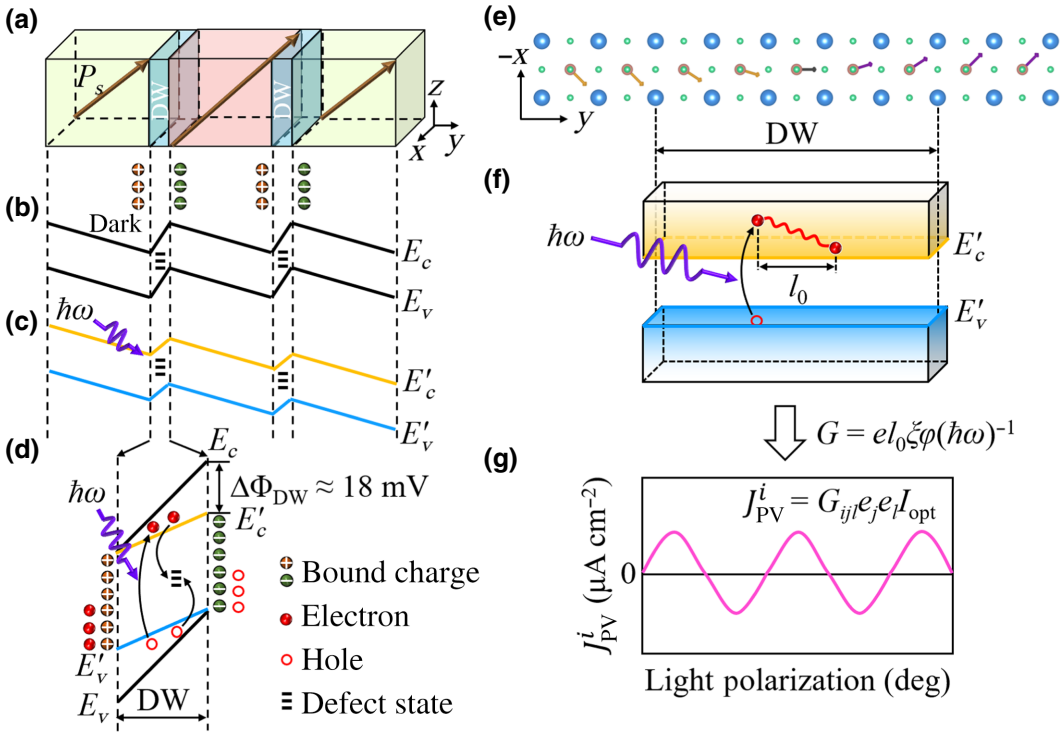

FIG. 5. Modeling of the mechanism of APV effect at DWs. (a) Schematic of three domains (two DWs) in MD sample. P_S denotes the ferroelectric spontaneous polarization in each domain. (b) Corresponding electronic band diagram showing the conduction-band minimum (E_c) and valence-band maximum (E_v) across these domains and DWs in the dark. (c) Evolution of band structure under illumination. E'_c and E'_v denote the conduction-band minimum and valence-band maximum under illumination. Wall width is exaggerated for clarity. (d) Schematic of band evolution, carrier generation, and combination at DW under illumination. (e) The atomic model at DW of MD sample projected on the z axis. (f) Anisotropic photogenerated carrier momentum distribution in DW corresponding to the (g) BPV effect. G is the amplitude of the third-rank piezoelectric tensor G_{ijl} component, e is the elementary charge, l_0 is the shift in space, ξ is the excitation asymmetry parameter, φ is the quantum yield, $\hbar\omega$ is the photon energy, e_j and e_l are the components of the light polarization vector.

In addition, we infer that the local BPV component in the 71° DW regions contributes to the observed $\beta^{DW}_{y,MD,amp}$ behavior. The lattice in the 71° DW regions is subject to a strong ferroelastic distortion caused by a spatial rotation of ferroelectric polarization [Fig. 5(e)], which is quite different from that in the domains. This spatial symmetry breaking at the DW provides a stronger local BPV component than in the domain interior and thus the resultant photocurrent shows the θ-dependent behavior. From the perspective of the microscopic origin of the BPV effect, the shift current and ballistic current mechanisms have been previously reported [30–33]. The shift current model is considered as one of the dominant microscopic mechanisms of the BPV effect. It points out that the shift current results from the coherent quantum wave-packet evolution during the absorption process. Shift current is a pure excitation theory and the kinetic process of photoexcited carriers (the relaxation, scattering, and recombination) are not taken into account. Ballistic current originates from asymmetric scattering of photoexcited carriers in momentum space, and is also viewed as a dominant microscopic mechanism for the BPV effect. Phonon scattering is the most
significant scattering source in ballistic current theory. Recent theoretical and experimental studies find that the ballistic current is comparable to shift current and both contribute to the BPV effect [33,34]. Figure 5(f) shows the microscopic schematic of the BPV effect in the DW region. The photogenerated carriers lose energy and fall to the bottom of the conduction band, leading to a shift l_0 in space. As a result, the amplitude of the tensor component $G = el_0\xi\varphi(\hbar\omega)^{-1}$, where e, ξ, φ, and $\hbar\omega$ are the elementary charge, excitation asymmetry parameter, quantum yield, and photon energy, and a steady-state current $J^i_{PV} = G_{ijl}e_j e_l I_{opt}$ is generated at the DW [Fig. 5(g)], where G_{ijl}, e_j, and e_l are the third-rank piezoelectric tensor and the components of the light polarization vector. Our experimental results also demonstrate that the BPV effect at the DW region is insensitive to defect concentration, which implies that phonon scattering dominates the asymmetric scattering process. Additionally, the polarized light illumination is high injection (35 W cm^{-2}).

Under the high-injection condition, defect states at the DW region are occupied by photoexcited carriers and thus defect scattering becomes negligible, especially for the case of BFO/STO. Thus, the APV effect of DWs, involving the larger effective field and the stronger local BPV component, provides a reasonable explanation for the PV behavior of the BFO films with stripe DWs.

III. CONCLUSION

In summary, we demonstrate the crucial role that the stripe-patterned DWs play in the PV properties of ferroelectric BFO films. The APV behavior of DWs in BFO films can be well explained by the combination of DWPV and BPV effects. The DWPV effect originates from the extremely strong built-in electric field at the DWs and gives rise to a markedly high photovoltage of the ferroelectric device, especially for periodic stripe DWs. However, defect states at DWs cause recombination of the photogenerated carriers and strongly decrease the photovoltage at DWs for the nonperiodic stripe DWs. The enhanced BPV effect of DWs, arising from the high degree of noncentrosymmetry at DWs, is about 25 times higher than that inside the domain, and it is nearly unaffected by defect states at DWs. This study quantitatively elucidates the APV effect of ferroelectric DWs in BFO films, opening up the possibility of designing DW optoelectronic devices.

ACKNOWLEDGMENTS

The work was supported by the National Natural Science Foundation of China (Grants No. 61574057, No. 61874045, and No. 61974042), and the Opening Project of Key Laboratory of Inorganic Functional Materials and Devices, Chinese Academy of Sciences (Grant No. KLIFMD202103). We are grateful to Professor Wei Bai for his technical support on the temperature-dependent BPV measurement. We also thank Professor Andrew M. Rappe and Professor Shi-jing Gong for the fruitful discussion on the BPV effect mechanism of domain walls.

APPENDIX: EXPERIMENT DETAILS

1. Device fabrication

Nominally 200-nm thick (001)-oriented BFO films are deposited on STO (100) substrates by PLD at 700 °C in 13 Pa oxygen pressure. The laser energy density is 1 J cm^{-2}, and the laser repetition rate is 10 Hz. We use the (110)-oriented DSO and $STO_{4^\circ\,[100]}$ substrates to control domain structures, respectively. To get 71° DWs, DSO substrates are annealed at 1000 °C for 2 h in the air. The buffered HF acid-etch and thermal treatment processes are used to obtain fully TiO_2-terminated surfaces on the STO substrate, resulting in atomically flat terraces. For obtaining the SD structure, we fabricate the BFO thin films on $STO_{4^\circ\,[110]}$ substrates. Aurum electrodes (50×500 μm^2) with variable interelectrode distances (20–200 μm) are fabricated by thermal evaporation using photolithography and lift-off processes.

2. Quantitative analysis of APV effects at DWs

First, we obtain the BPV tensor (β_{15}, β_{22}, β_{31}, and β_{33}) by fitting the BPV effect of the SD sample. Then, the BPV effect of the MD sample is theoretically calculated, which considers that the 71° domain of the MD sample consists of two kinds of rhombohedral unit cells. The APV effect at the DWs is finally quantified by subtracting the theoretically calculated BPV effect from the experimental PV result of the MD sample.

3. Materials and device characterization

The crystalline phase of BFO films is determined by XRD analysis (D8 DISCOVER, Bruker). The domain structures of the BFO thin films are confirmed by PFM (Cypher, Asylum Research) and RSM (D8 DISCOVER, Bruker) measurements. The MD-STO and MD-DSO samples are processed into cross-section samples using the focused-ion-beam technique in the FEI Helios G4 system. The STEM experiments are carried out with a JEM Grand ARM 300F microscope operating at 300 kV in the STEM mode. To measure the PV effect of the BFO samples, we use a linearly polarized laser with a wavelength of 405 nm ($h\upsilon = 3.06$ eV). The angle of polarized light is varied by a half-wavelength plate. The PV response is characterized by current-voltage measurements using a high-input impedance electrometer (Keithley 2636). To eliminate the pyroelectric effect, current-voltage data are collected after sufficient illumination time (around 20 min). In addition, the entire measurement process takes about 60 min. Therefore, the current-voltage characteristics are steady state.

[1] D. V. D. Linde, A. M. Glass, and K. F. Rodgers, Multiphoton photorefractive processes for optical storage in $LiNbO_3$, Appl. Phys. Lett. **25**, 155 (1974).
[2] A. Kholkin, O. Boiarkine, and N. Setter, Transient photocurrents in lead zirconate titanate thin films, Appl. Phys. Lett. **72**, 130 (1998).
[3] M. Qin, K. Yao, and Y. C. Liang, High efficient photovoltaics in nanoscaled ferroelectric thin films, Appl. Phys. Lett. **93**, 122904 (2008).
[4] S. Y. Yang, J. Seidel, S. J. Byrnes, P. Shafer, C. H. Yang, M. D. Rossell, P. Yu, Y. H. Chu, J. F. Scott, J. W. Ager, *et al.*, Above-bandgap voltages from ferroelectric photovoltaic devices, Nat. Nanotechnol. **5**, 143 (2010).
[5] R. Inoue, S. Takahashi, Y. Kitanaka, T. Oguchi, Y. Noguchi, and M. Miyayama, Enhanced photovoltaic currents in strained Fe-doped $LiNbO_3$ films, Phys. Status Solidi A **212**, 2968 (2015).

[6] M. MinYang, Z. DongLuo, D. J. Kim, and M. Alexe, Bulk photovoltaic effect in monodomain $BiFeO_3$ thin films, Appl. Phys. Lett. **110**, 183902 (2017).

[7] W. Ji, K. Yao, and Y. C. Liang, Evidence of bulk photovoltaic effect and large tensor coefficient in ferroelectric $BiFeO_3$ thin films, Phys. Rev. B **84**, 094115 (2011).

[8] H. Matsuo, Y. Noguchi, and M. Miyayama, Gap-state engineering of visible-light-active ferroelectrics for photovoltaic applications, Nat. Commun. **8**, 207 (2017).

[9] R. Inoue, S. Ishikawa, R. Imura, Y. Kitanaka, T. Oguchi, Y. Noguchi, and M. Miyayama, Giant photovoltaic effect of ferroelectric domain walls in perovskite single crystals, Sci. Rep. **5**, 14741 (2015).

[10] A. Bhatnagar, A. Roy Chaudhuri, Y. Heon Kim, D. Hesse, and M. Alexe, Role of domain walls in the abnormal photovoltaic effect in $BiFeO_3$, Nat. Commun. **4**, 2835 (2013).

[11] J. Seidel, L. W. Martin, Q. He, Q. Zhan, Y. H. Chu, A. Rother, M. E. Hawkridge, P. Maksymovych, P. Yu, M. Gajek, *et al.*, Conduction at domain walls in oxide multiferroics, Nat. Mater. **8**, 229 (2009).

[12] J. Guyonnet, I. Gaponenko, S. Gariglio, and P. Paruch, Conduction at domain walls in insulating $Pb(Zr_{0.2}Ti_{0.8})O_3$ thin films, Adv. Mater. **23**, 5377 (2011).

[13] J. Allibe, S. Fusil, K. Bouzehouane, C. Daumont, D. Sando, E. Jacquet, C. Deranlot, M. Bibes, and A. Barthélémy, Room temperature electrical manipulation of giant magnetoresistance in spin valves exchange-biased with $BiFeO_3$, Nano Lett. **12**, 1141 (2012).

[14] H. Matsuo, Y. Noguchi, M. Miyayama, T. Kiguchi, and T. J. Konno, Enhanced photovoltaic effects in ferroelectric solid solution thin films with nanodomains, Appl. Phys. Lett. **116**, 132901 (2020).

[15] Y. Noguchi, R. Inoue, and H. Matsuo, Domain-wall photovoltaic effect in Fe-doped $BaTiO_3$ single crystals, J. Appl. Phys. **129**, 084101 (2021).

[16] H. Matsuo, Y. Kitanaka, R. Inoue, Y. Noguchi, M. Miyayama, T. Kiguchi, and T. J. Konno, Bulk and domain-wall effects in ferroelectric photovoltaics, Phys. Rev. B **94**, 214111 (2016).

[17] B. Guzelturk, A. B. Mei, L. Zhang, L. Z. Tan, P. Donahue, A. G. Singh, D. G. Schlom, L. W. Martin, and A. M. Lindenberg, Light-induced currents at domain walls in multiferroic $BiFeO_3$, Nano Lett. **20**, 145 (2020).

[18] See the Supplemental Material at http://link.aps.org/supplemental/10.1103/PhysRevApplied.19.024050 for PFM and XRD results (Sec. S1), PV properties of SD samples (Fig. S2), J-V_{bias} results under different light intensities (Fig. S3), J-V_{bias} results for different polarization light angles (Fig. S4), calculation of BPV tensor and photovoltaic current in BFO films (Sec. S2), J-V_{bias} results under white light illumination (Fig. S6), PV measurement along the y axis under 405-nm monochromatic light (Sec. S3), STEM results of BFO films (Fig. S8), STEM and GPA results of BFO films (Fig. S9), temperature-dependent PV studies (Sec. S4), and analysis of the proposed model and calculation of J_{SC} (Sec. S5), which also includes Refs. [35–40].

[19] P. Yu, W. Luo, D. Yi, J. X. Zhang, M. D. Rossell, C.-H. Yang, L. You, G. S. Bhalla, S. Y. Yang, Q. He, *et al.*, Interface control of bulk ferroelectric polarization, Proc. Natl. Acad. Sci. U. S. A. **109**, 9710 (2012).

[20] G. De Luca, N. Strkalj, S. Manz, C. Bouillet, M. Fiebig, and M. Trassin, Nanoscale design of polarization in ultrathin ferroelectric heterostructures, Nat. Commun. **8**, 1419 (2017).

[21] Y. Zhang, H. Lu, X. Yan, X. Cheng, L. Xie, T. Aoki, L. Li, C. Heikes, S. P. Lau, D. G. Schlom, *et al.*, Intrinsic conductance of domain walls in $BiFeO_3$, Adv. Mater. **31**, 1902099 (2019).

[22] J. Nelson, *The physics of solar cells* (Imperial College Press, London, 2003).

[23] C. T. Nelson, B. Winchester, Y. Zhang, S. J. Kim, A. Melville, C. Adamo, C. M. Folkman, S. H. Baek, C. B. Eom, D. G. Schlom, *et al.*, Spontaneous vortex nanodomain arrays at ferroelectric heterointerfaces, Nano Lett. **11**, 828 (2011).

[24] L. Li, P. Gao, C. T. Nelson, J. R. Jokisaari, Y. Zhang, S. J. Kim, A. Melville, C. Adamo, D. G. Schlom, and X. Pan, Atomic scale structure changes induced by charged domain walls in ferroelectric materials, Nano Lett. **13**, 5218 (2013).

[25] W. Y. Wang, Y. L. Tang, Y. L. Zhu, Y. B. Xu, Y. Liu, Y. J. Wang, S. Jagadeesh, and X. L. Ma, Atomic level 1D structural modulations at the negatively charged domain walls in $BiFeO_3$ films, Adv. Mater. Interfaces **2**, 1500024 (2015).

[26] Y. Liu, Y. L. Zhu, Y. L. Tang, Y. J. Wang, Y. X. Jiang, Y. B. Xu, B. Zhang, and X. L. Ma, Local enhancement of polarization at $PbTiO_3/BiFeO_3$ interfaces mediated by charge transfer, Nano Lett. **17**, 3619 (2017).

[27] A. Kontsos and C. M. Landis, Computational modeling of domain wall interactions with dislocations in ferroelectric crystals, Int. J. Solids Struct. **46**, 1491 (2009).

[28] A. Tselev, P. Yu, Y. Cao, L. R. Dedon, L. W. Martin, S. V. Kalinin, and P. Maksymovych, Microwave a.c. conductivity of domain walls in ferroelectric thin films, Nat. Commun. **7**, 11630 (2016).

[29] L. Li, J. R. Jokisaari, Y. Zhang, X. Cheng, X. Yan, C. Heikes, Q. Lin, C. Gadre, D. G. Schlom, L. Q. Chen, *et al.*, Control of domain structures in multiferroic thin films through defect engineering, Adv. Mater. **30**, 1802737 (2018).

[30] S. M. Young and A. M. Rappe, First Principles Calculation of the Shift Current Photovoltaic Effect in Ferroelectrics, Phys. Rev. Lett. **109**, 116601 (2012).

[31] S. M. Young, F. Zheng, and A. M. Rappe, First-Principles Calculation of the Bulk Photovoltaic Effect in Bismuth Ferrite, Phys. Rev. Lett. **109**, 236601 (2012).

[32] A. Zenkevich, Y. Matveyev, K. Maksimova, R. Gaynutdinov, A. Tolstikhina, and V. Fridkin, Giant bulk photovoltaic effect in thin ferroelectric $BaTiO_3$ films, Phys. Rev. B **90**, 161409 (2014).

[33] Z. Dai, A. M. Schankler, L. Gao, L. Z. Tan, and A. M. Rappe, Phonon-Assisted Ballistic Current from First-Principles Calculations, Phys. Rev. Lett. **126**, 177403 (2021).

[34] A. M. Burger, R. Agarwal, A. Aprelev, E. Schruba, A. Gutierrez-Perez, V. M. Fridkin, and J. E. Spanier, Direct observation of shift and ballistic photovoltaic currents, Sci. Adv. **5**, eaau5588 (2019).

[35] K. v. Benthem, C. Elsässer, and R. H. French, Bulk electronic structure of $SrTiO_3$: Experiment and theory, J. Appl. Phys. **90**, 6156 (2001).

[36] C. A. Mizzi, P. Koirala, A. Gulec, and L. D. Marks, Charging ain't all bad: Complex physics in $DyScO_3$, Ultramicroscopy **203**, 119 (2019).

[37] S.-J. Gong, F. Zheng, and A. M. Rappe, Phonon Influence on Bulk Photovoltaic Effect in the Ferroelectric Semiconductor GeTe, Phys. Rev. Lett. **121**, 017402 (2018).

[38] T. Choi, S. Lee, Y. J. Choi, V. Kiryukhin, and S.-W. Cheong, Switchable ferroelectric diode and photovoltaic effect in $BiFeO_3$, Science **324**, 63 (2009).

[39] J. Seidel, D. Fu, S.-Y. Yang, E. Alarcón-Lladó, J. Wu, R. Ramesh, and J. W. Ager, Efficient Photovoltaic Current Generation at Ferroelectric Domain Walls, Phys. Rev. Lett. **107**, 126805 (2011).

[40] J. Lin, P. Shen, Y. Liu, F. Yue, Y. Chen, Z. Zhou, P. Yang, J. Chu, C.-G. Duan, and L. Sun, Electric-field modulated photovoltaic effect of ferroelectric double-perovskite Bi_2FeMnO_6 films, Appl. Phys. Lett. **119**, 102903 (2021).